Hollowing of MnO Nanocrystals Triggered by Metal Cation Replacement: Implications for the Electrocatalytic Oxygen Evolution Reaction

Hollowing of MnO Nanocrystals Triggered by Metal Cation Replacement: Implications for the Electrocatalytic Oxygen Evolution Reaction

Chunzheng Wu,* Zhiya Dang,* Lea Pasquale, Mengjiao Wang, Massimo Colombo, Luca De Trizio,* and Liberato Manna

Abstract: Manganese oxide (MnO_x) based hollow nanocrystals (NCs) represent a promising class of materials for catalysis. The conventional routes to synthesize such nanostructures rely on the use of hard/soft sacrificial templates or on high reaction temperatures. Herein, we report a template-free method to rapidly transform nonhollow MnO NCs into hollow nanostructures at room temperature. Our synthesis method is based on the reaction of guest metal cations $M^{\delta+}$ (e.g., Fe^{2+}, Ce^{3+}, Fe^{3+}, etc.) with MnO NCs, the latter being actually passivated by a thin Mn_3O_4 layer. The guest cations replace part of the Mn ions in the Mn_3O_4 shell up to a critical threshold value (e.g., ∼12 at. % when working with Fe^{2+} guest cations), above which etching of the MnO core rapidly occurs. Our analyses suggested that the etching of the core could be related to the release of strain that is built up between the MnO core and the $Mn_{3-x}M_xO_4$ shell as the exchange progresses. When Fe^{2+} ions are employed as guest cations, the resulting $Mn_{3-x}Fe_xO_4$ hollow NCs exhibit high activity in the electrocatalytic oxygen evolution reaction due to their large electrochemical surface area and low charge transfer resistance. Our work provides an easy and green synthesis strategy to prepare hollow NCs with control over the composition and size, which are features that make them efficient electrocatalysts.

KEYWORDS: hollow nanocrystals, manganese oxide, Fe doping, galvanic replacement, oxygen evolution reaction

1. INTRODUCTION

Hollow micro- or nanostructures are characterized by a large internal void space, hence a very large surface to volume ratio and good volume flexibility.1,2 Such features have been exploited in catalysis,3-6 energy storage,7-10 and biomedicine.11,12 Among the different materials prepared in a hollow form, manganese oxides have shown excellent performance in the above-mentioned applications.11-14 Hollow MnOx particles are generally prepared with the use of sacrificial hard or soft templates such as carbon,15 SiO2,16 and vesicles/micelles.17 The use of such templates makes the synthesis of hollow structures elaborate as one needs to produce the template and, at a later stage, to remove it, additionally causing a waste of materials. Alternatively, template-free methods, based either on the Kirkendall effect13,18 or on the galvanic replacement,19-21 have been used to generate cavities directly inside MnO x nanocrystals (NCs). The Kirkendall effect

consists of a fast outward-diffusion of “host” atoms from preformed NCs and a concomitant slow inward-diffusion of “guest” atoms, resulting in the formation of hollow structures.[22,23] In the galvanic replacement reaction, in turn, the difference in electrochemical potential between “host” and “guest” metal ions leads to their exchange (i.e., “host” cations of preformed NCs are oxidized/reduced and dissolved in solution, while “guest” cations present in the solution are reduced/oxidized and deposit on the surface of NCs), producing, in some cases, hollow structures.[19,24,25] However, the synthesis of hollow MnOx NCs via these processes requires relatively high temperatures and a large amount of guest ions.[3,13,18-21] For example, the Kirkendall process involving MnO NCs and trioctylphosphine oxide to prepare hollow MnOxPy nanoparticles only occurs at 300 °C with P/Mn ratios larger than 1,18 while the galvanic replacement reaction between Mn_3O_4 NCs and Fe^{2+} ions, to produce hollow $Mn_{3-x}Fe_xO_4$ NCs, occurs at 90 °C with Fe% ≥ 60 at. %.[19,20] Working at lower temperatures or using a smaller amount of reaction precursors often lead to an incomplete hollowing process, which can then limit the performance of the resulting NCs in different applications.[3]

Herein, we report a facile method to convert initial nonhollow MnO NCs (supported on SiO_2) into hollow nanostructures at room temperature. This is achieved by a simple treatment of MnO NCs, encased by a thin Mn_3O_4 shell, with diluted aqueous solutions of metal cations (such as Fe^{2+}, Ce^{3+}, and Fe^{3+}), which trigger either a galvanic replacement or a cation exchange reaction within the Mn_3O_4 shell. Our results point to a hollowing mechanism that is strongly related to the strain that is built up between the MnO core and the thin Mn_3O_4 shell as the exchange progresses. Among the different hollow nanostructures obtained in this work, those prepared by employing Fe^{2+} guest cations, namely $Mn_{3-x}Fe_xO_4$ hollow NCs, were tested in the electrocatalytic oxygen evolution reaction (OER). These NCs revealed a lower overpotential and faster reaction kinetics compared not only to the original MnO NCs, but also to the state-of-the-art MnxOy and FexOy based electrocatalysts.

■ EXPERIMENTAL METHODS

Chemicals. Manganese(II) nitride tetrahydrate ($Mn(NO_3)_2 \cdot 4H_2O$), oleic acid (technical grade, 90%), 1-octadecene (technical grade, 90%), iron(II) perchlorate hydrate ($Fe(ClO_4)_2 \cdot xH_2O$), iron-(III) perchlorate hydrate ($Fe(ClO_4)_3 \cdot xH_2O$), cerium chloride heptahydrate ($CeCl_3 \cdot 7H_2O$) were purchased from Sigma-Aldrich. Hexane, hydrochloric acid (≥37%) and ethanol were purchased from Fluka. Sodium hydroxide (pellets, NaOH, 98%) was purchased from Panreac AppliChem. Hydrophilic fumed silica (AEROSIL-380) was purchased from Evonik Industries. All the chemicals were used without further purification. Ultrapure Milli-Q (18.2 MΩ·cm) was used as water source.

Preparation of the SiO_2-Supported MnO (MnO/SiO_2)

Sample. MnO NCs were prepared through a thermal decomposition of Mn-oleate, as reported by Schladt et al.26 Then, a colloidal deposition method was used to prepare the MnO/SiO_2. Typically, 2.2 g of fumed SiO_2 was dispersed in 600 mL of hexane, and a hexane solution of MnO (targeting at a Mn concentration of 2-15 wt %) was added to the mixture dropwise under stirring. The mixture was then sonicated for 30 min to improve the NCs dispersion. The products were collected by centrifugation and dried at 60 °C overnight.

Hollowing Process. One hundred fifty mg of the MnO/SiO_2 sample were dispersed in 75 mL of H_2O with sonication. The mixture was stirred in N_2 for 30 min to remove air. Fifteen mL of $Fe(ClO_4)_2$ aqueous solution with various concentrations (5% to 30% at. with respect to the Mn atoms) was then injected to the above mixture. After reacting for 90 min in N_2, the product was collected by centrifugation, washed twice with H_2O, and washed once with ethanol. Finally, the sample was dried at 60 °C overnight. The sample was named MnO/SiO_2-xFe^{2+}, where x is the ratio of injected Fe atoms and the total Mn atoms in the sample. The Ce^{3+} and Fe^{3+} treatments were performed in the same way as for the Fe^{2+} treatment, except that $Ce(NO_3)_3$ and $Fe(ClO_4)_3$ were used as the metal precursors. The obtained samples were named MnO/SiO_2-xCe^{3+} and MnO/SiO_2-xFe^{3+} accordingly.

Material Characterizations. Bright-field transmission electron microscopy (TEM) images were recorded using a JEOL JEM-1011 instrument with a thermionic W source operating at 100 kV, for which samples were prepared by dropping solutions onto carbon-coated 200 mesh copper grids. High-resolution TEM (HRTEM), high angular annular scanning-TEM (HAADF-STEM) and energy-dispersive X-ray

spectroscopy (EDS) measurements were conducted with a JEOL JEM-2200FS microscope, for which the samples were deposited on ultrathin carbon/holey carbon-coated 400 mesh copper grids, and then annealed in vacuum at 100 °C for 1 h to remove the water residuals. This microscope is equipped with a 200 kV field emission gun, a CEOS spherical aberration corrector for the objective lens, an in-column image filter (Ω-type), enabling a spatial resolution of 0.9 Å, and a Quantax 400 system and a XFlash 5060 silicon-drift detector (SDD, 60 mm2 active area) for the EDS analysis. The reported EDS maps were obtained by integrating the Mn Kα, Fe Kα, and Si Kα peaks in the spectra. The X-ray diffraction (XRD) measurements were performed using a PANalytical Empyrean X-ray diffractometer equipped with a 1.8 kW Cu Kα ceramic X-ray tube and a PIXcel3D 2 × 2 area detector, operating at 45 kV and 40 mA. The diffraction patterns were collected in parallel-beam (PB) geometry and symmetric reflection mode using a zero-diffraction silicon substrate. The chemical composition of the catalysts was measured by inductively coupled plasma optical emission spectroscopy (ICPOES) using an iCAP 6000 Thermo Scientific spectrometer. The X-ray photoelectron spectroscopy (XPS) characterizations were performed on a Kratos Axis UltraDLD spectrometer using a monochromatic Al Kα source (15 kV, 20 mA), and the binding energy was calibrated by setting the main C 1s peak (corresponding to C-C bonds) to 284.8 eV. The thermogravimetric analysis (TGA) was performed using a TGA Q500 instrument, and the temperature was varied from room temperature to 600 °C with a heating rate of 5 °C/min in air flux. Scanning electron microscopy (SEM) and EDS mapping were performed using a FEI Quanta FEG 250 instrument.

Electrocatalytic Tests. The electrodes were prepared by loading MnO colloidal NCs onto nickel foam, followed by an in situ transformation by adding an aqueous solution of Fe2+. In detail, a certain amount of hexane solution of MnO NCs (contained 1 mg of Mn) was dropped onto a nickel foam with a size of 10 mm × 10 mm × 1.5 mm (Guang Sheng Jia New Materials Co., Ltd.) and dried naturally in air. This nickel foam was then immersed into 10 mL of water containing a certain amount of Fe(ClO4)2 for 90 min. Before the electrocatalytic tests, all the electrodes were calcined in air at 450 °C for 2 h to remove the ligands. The electrocatalytic OER was carried out at room temperature (i.e., 25 °C) on an electrochemical station (CHI660C) in a standard three-electrode system: our sample as the working electrode, a 10 mm × 10 mm Pt net as the counter

electrode, and a standard Ag/AgCl electrode as the reference electrode, and a 1 M KOH solution (pH = 14) as the electrolyte. The OER polarization curve measurements were performed by linear sweep voltammetry (LSV) at a scan rate of 5 mV/s. Electrochemical impedance spectra (EIS) were measured at an overpotential of 500 mV from 0.01 Hz to 100 kHz with an amplitude of 5 mV. The electrochemical double layer capacitance (Cdl) was measured by scanning cyclic voltammetry (CV) at a voltage ranging from 0.15 to 0.30 V (vs Ag/AgCl) at scan speeds of 10, 20, 30, 40, and 50 mV/s. All the polarization curves reported here were corrected with iR compensation.

■ RESULTS AND DISCUSSION

The as-synthesized MnO NCs (reported in Supporting Information (SI) Figure S1) had a spherical morphology and a rather narrow size distribution, with an average diameter of ∼20 nm. Considering that the organic ligands (i.e., oleic acid) passivating the surface of these MnO NCs hinder their dispersion in water, amorphous SiO_2 was selected in this work as a hydrophilic support for the MnO NCs, as it enables them to be dispersed in aqueous solutions of guest metal cations while preventing their aggregation. Figure 1a is a TEM image of the starting MnO NCs on the amorphous SiO_2 support (with a Mn loading of 12 wt %, see also sketch in the inset), while Figure 1b is a representative HAADF-STEM image of a MnO NC: as revealed by the intensity contrast (Figure 1b) and the corresponding intensity profile (Figure 1c) the MnO NC had a core-shell structure with a ∼10 nm dense core and a ∼2-4 nm-thick shell with relatively lower density. Additionally, our XRD analysis (Figure 2a, orange pattern) indicated the presence of both a predominant MnO cubic phase (ICSD number 29326) and a minor fraction of a Mn_3O_4 tetragonal phase (ICSD number 68174). The data suggested that the surface of the starting MnO NCs was oxidized upon exposure to air, forming a Mn_3O_4 layer, in accordance with what reported in several works.[11,27] For convenience, we will refer to these NCs as MnO NCs throughout this work.

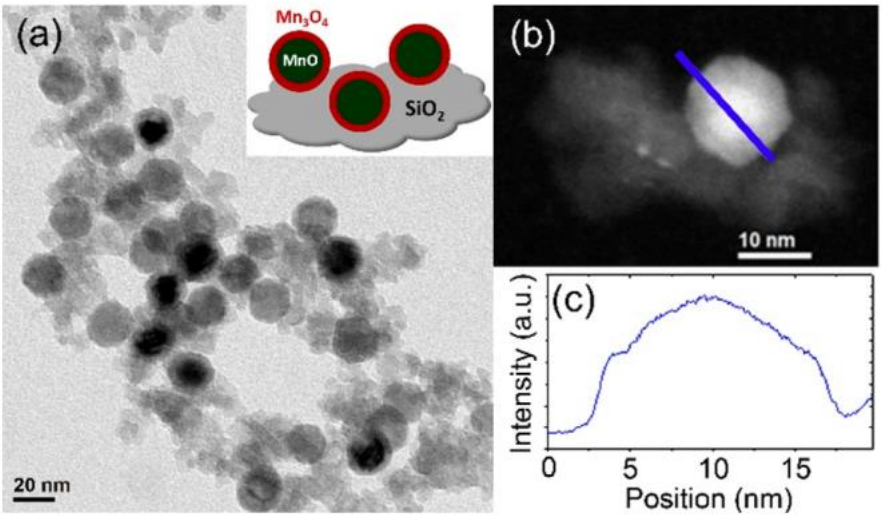

Figure 1. (a) Typical bright field TEM image of the MnO/SiO2 sample. The inset is a schematic representation of the MnO-Mn3O4 core-shell structures. (b) HAADF-STEM image and (c) the intensity profile across a MnO NC along the blue line showing the core having a higher intensity than the shell.

We then studied the effects of exposing our MnO NCs to aqueous solutions containing different metal cations, namely Fe2+, Ce3+, or Fe3+. Here, we will first focus our discussion on the experiments involving Fe2+ cations as the exemplary case study. MnO/SiO2 samples were dispersed in aqueous solutions containing different amounts of Fe2+ cations, ranging from 5% to 30% at.% with respect to the Mn atoms, and the corresponding products were named MnO/SiO2-xFe2+ (where x is the at.%). According to the TEM analysis, the starting MnO NCs underwent a hollowing process whose extent depended on the Fe2+ concentration (Figure 2b-d). In details, when using a 5% Fe2+ solution, TEM analysis of the resulting product (MnO/SiO2-5Fe2+) indicated that only a minor portion of the NCs was hollow (Figure 2b). Based on the XRD analysis (Figure 2a, red pattern), the NCs exhibited a cubic MnO structure, with minor reflections corresponding to the tetragonal Mn3O4 shell, and their overall XRD pattern was not much different from that to the starting NCs (Figure 2a, orange pattern). When working with a 10% Fe2+ solution (sample MnO/SiO2-10Fe2+), most of the NCs turned into hollow, while only a small portion remained nonhollow (Figure 2c). The XRD pattern of such sample indicated a substantial drop in the MnO/Mn3O4 peaks intensity ratio (Figure 2a, blue pattern). When the concentration of Fe2+ was

as high as 30%, the resulting MnO/SiO2-30Fe2+ sample was composed of hollow NCs having a higher porosity with respect to the samples prepared at lower Fe2+ concentrations (Figure 2d), and it was characterized by very weak and broad XRD reflections which could be indexed with the Mn3O4 structure (Figure 2a, magenta pattern). Noteworthy, the hollowing transformation occurred rapidly (within 1 min) in all the cases discussed above, after which no noticeable morphological change was observed (SI Figure S2). A control experiment performed on a ligand-free MnO/SiO2 sample (that is, a sample in which the oleic acid passivating the starting NCs was removed, SI Figure S3) showed that the surface ligands did not affect this transformation.

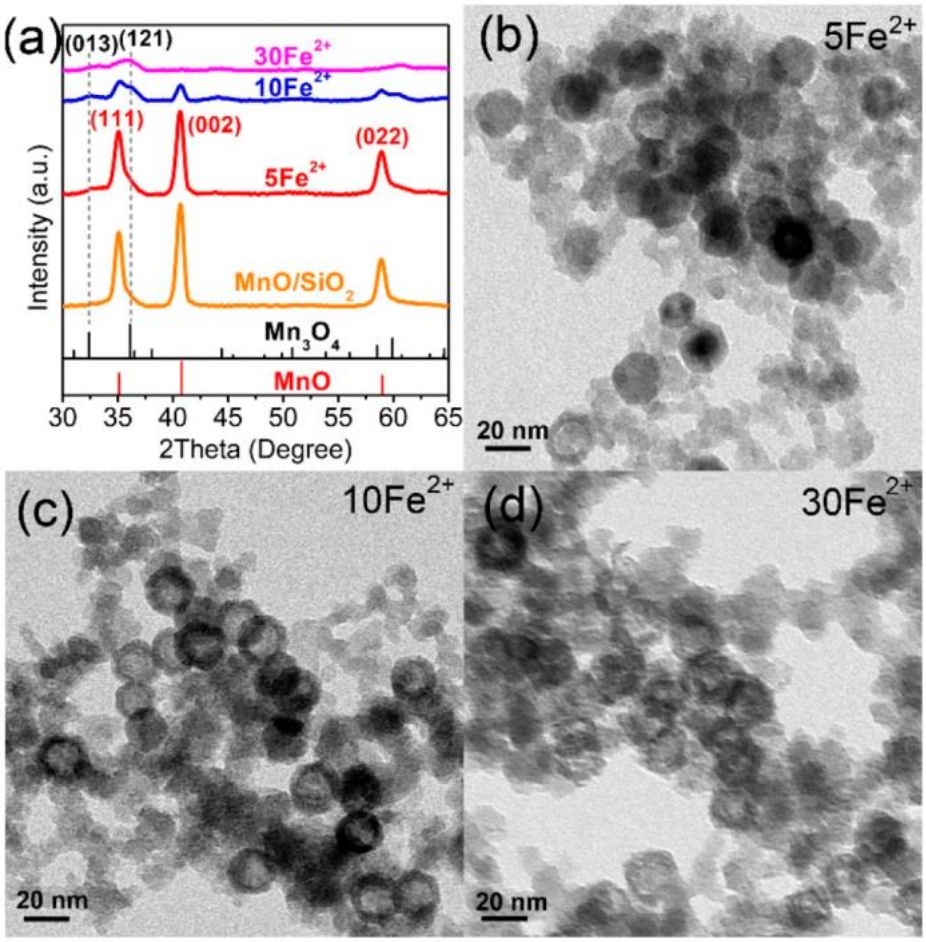

Figure 2. (a) XRD patterns of MnO/SiO2 before and after Fe2+ treatments together with the reference bulk reflections of MnO (ICSD: 29326) and Mn3O4 (ICSD: 68174) crystal structures. The broad XRD peak at 20° characterizing the amorphous fumed SiO2 substrate has been subtracted for clarity. TEM images of (b) MnO/

SiO2-5Fe2+, (c) MnO/SiO2-10Fe2+, (d) MnO/SiO2-30Fe2+ samples.
The elemental analysis of the samples, performed via ICPOES, revealed that the overall amount of Fe, calculated as the Fe/(Fe+Mn) molar ratio, increased linearly with the amount of Fe2+ employed in the reaction (Table 1), indicating that the morphological transformation was accompanied by a Fe → Mn substitution process. According to our XPS analysis, the Fe cations inside the hollow nanostructures had a + 3 oxidation state (SI Figure S4).

Table 1. Composition of MnO/SiO2 and MnO/SiO2-xFe2+ (x = 5, 10, or 30)

samples	Mn (wt.%)	Fe (wt.%)	Fe/(Fe+Mn) (at.%)	D_{MnO} (nm)[a]
MnO/SiO_2	12.00			15.7
MnO/SiO_2-$5Fe^{2+}$	11.41	0.63	5.5	15.0
MnO/SiO_2-$10Fe^{2+}$	10.26	1.22	9.6	14.2
MnO/SiO_2-$30Fe^{2+}$	7.49	3.40	30.6	

aDMnO is the average diameter of MnO NCs, calculated through Sherrer equation by using the full width at half-maximum (fwhm) of the XRD peak at 2θ = 40.8°.
HRTEM and STEM-EDS analyses were then performed to elucidate the atomic structure and composition of the samples obtained. We start with the MnO/SiO2-10Fe2+ sample as it contains both hollow and nonhollow NCs. According to the STEM-EDS mapping, the nonhollow NCs exhibited a core-shell structure, with Fe species mostly distributed over a thin outer-layer around the NCs (Figure 3a): the measured Fe/(Fe +Mn) ratio was ∼11.4 at. % in the shell and ∼2.0 at. % in the core. Furthermore, the HRTEM analysis coupled with the corresponding strain map examination (Figure 3b) revealed that the core of the nonhollow NCs was composed of cubic MnO, while the shell had a structure resembling that of the tetragonal Mn3O4, but with slightly smaller lattice parameters. This would be consistent with the presence of a Mn3-xFexO4 structure containing Fe cations, which are smaller than Mn ones (the ionic radii of Fe2+ and Mn2+ in tetrahedral coordination are 0.77 and 0.83 Å, respectively, while the ionic radii of Fe3+ and Mn3+ in octahedral coordination are 0.65 and 0.72 Å, respectively28). The core and shell exhibited epitaxial relationships: MnO [001]‖ Mn3-xFexO4 [001] and MnO (110)‖ Mn3-xFexO4 (200). The hollow NCs present in

the same sample were found instead to contain both Fe and Mn distributed homogeneously in the hollow cage. The average Fe/(Fe+Mn) ratio in these NCs was ~11.6 at. %, that is, very close to that of the shell in the nonhollow NCs (Figure 3c). HRTEM analysis further revealed that the hollow cages are composed of nanocrystalline domains, whose structure can be tentatively indexed as tetragonal Mn3-xFexO4 (Figure 3d).

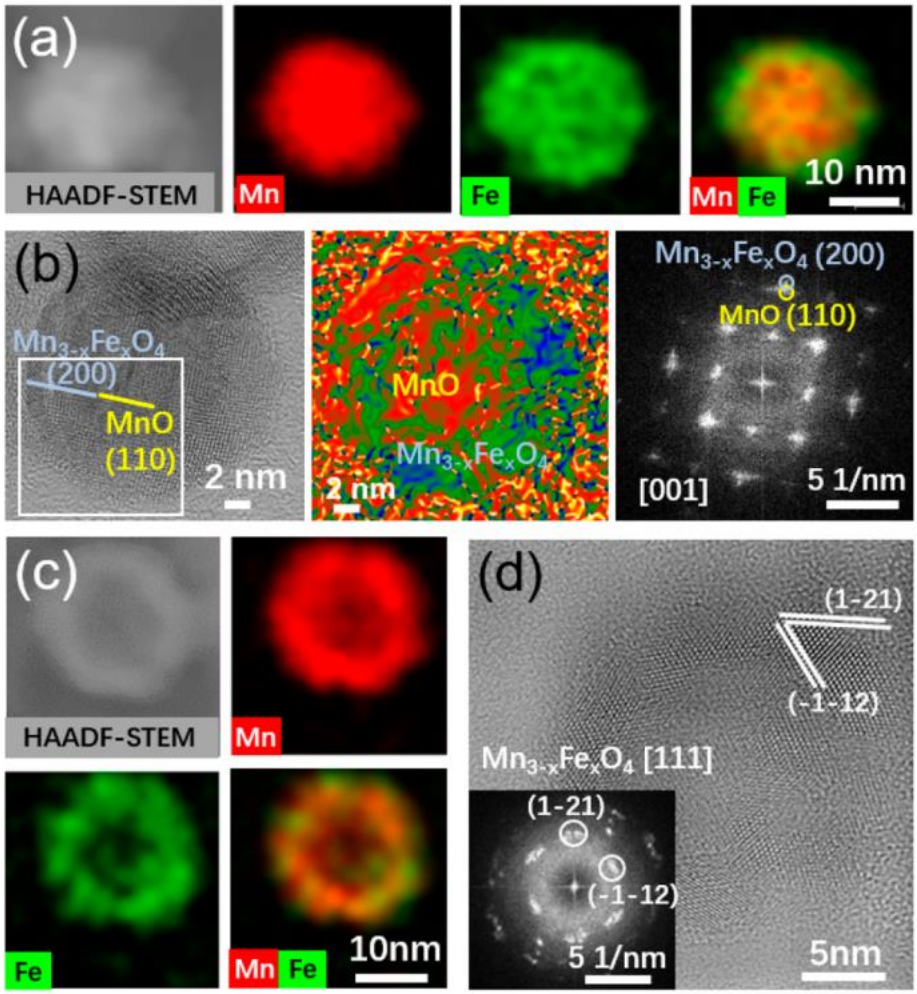

Figure 3. Transmission electron microscopy analysis of the MnO/SiO2-10Fe2+ sample: (a) STEM-EDS mapping of a nonhollow NC; (b) HRTEM, strain map and fast Fourier transform (FFT, of the white framed region) of a nonhollow NC; (c) STEM-EDS mapping of a hollow NC; (d) HRTEM and the corresponding FFT of a hollow NC.

In order to elucidate the underlying mechanism that is responsible for the formation of hollow Mn3-xFexO4 nanostructures, we performed several control experiments. We first prepared Mn3O4 NCs supported on SiO2 by fully oxidizing the initial MnO NCs at 450 °C in air. We then treated the sample with a solution of Fe2+ cations (420%

excess) at room temperature and analyzed the corresponding product. TEM and ICP analyses showed that the Mn ions of nonhollow Mn_3O_4 NCs can be indeed replaced by Fe^{2+} at room temperature (see the details in SI Figure S5 and Table S1). This occurs, most likely, through a galvanic replacement between trivalent Mn(III) in the Mn_3O_4 and Fe^{2+}, i.e., Mn(III) + Fe^{2+} → Mn^{2+} + Fe(III). Such galvanic replacement, described as an oxidation-reduction reaction, is driven by the higher reduction potential of Mn_3O_4/Mn^{2+} (1.82 eV) than that of Fe^{3+}/Fe^{2+} (0.77 V), analogously to what reported by Oh et al.[19] This observation, combined with the 3+ oxidation state of Fe in MnO/SiO_2-30Fe^{2+} (based on XPS analysis in SI Figure S4), suggest that the thin Mn_3O_4 layer on the surface of starting MnO NC underwent galvanic replacement with Fe^{2+} cations as well, forming a $Mn_{3-x}Fe_xO_4$ shell.

We then exposed a MnO/SiO_2 starting sample to a precalcination treatment (i.e., annealing at 120 °C under air), aiming at increasing the thickness of the Mn_3O_4 shell. The samples obtained in this way were immersed in an aqueous solution of Fe^{2+} cations (100%) and the resulting products were characterized via XRD and TEM analyses. As shown in SI Figure S6, starting from MnO NCs with thicker Mn_3O_4 shells (i.e., ∼ 10 nm), the product consisted of $Mn_{3-x}Fe_xO_4$ hollow structures having a wall-thickness of ∼10 nm. This result suggested that the thickness of the outer Mn_3O_4 shell governed the thickness of the final $Mn_{3-x}Fe_xO_4$ hollow NCs, and that, also in this case, the overall process consisted of a first step of Mn_3O_4 → $Mn_{3-x}Fe_xO_4$ shell conversion followed by the removal of the MnO core (Scheme 1). Moreover, the coreremoval occurred with no apparent variation of the size of the NCs: a statistical analysis of more than 100 hollow NCs in MnO/SiO_2-10Fe^{2+} sample revealed that their outer diameter (i.e., 20.9 ± 1.0 nm) was almost the same as that of the starting nonhollow MnO NCs (i.e., 21.0 ± 1.3 nm) (SI Figure S7).

We also tried to vary the solvent in which the Fe^{2+} treatment was carried out by using ethanol instead of water. In this solvent the kinetics of the galvanic replacement reaction was observed to occur slower and only a small fraction of the starting MnO NCs was converted into hollow nanostructures, even when working at a high Fe^{2+} content, i.e., 100 % of Fe^{2+} (SI Figure S8). STEM-EDS analyses of the Fe/(Fe+Mn) ratio of the nonhollow NCs in ethanol after the treatment turned out to be much lower (i.e., ∼4.0 at. %) compared to the nonhollow NCs in the MnO/SiO_2-10Fe^{2+} in water (i.e., ∼8.6 at. %). In contrast, the hollow NCs prepared in ethanol had a Fe/(Fe+Mn) ratio of 11.7 at. %, that is, very close to the value found for the hollow NCs obtained in water. These data overall suggest that, in order for the core to be removed, the

amount of Fe in the Mn_3O_4 layer has to overcome a critical value (i.e., ∼ 12 at. %, in other words, x in the $Mn_{3-x}Fe_xO_4$ shell must be above 0.36, see Scheme 1).

Upon closer examination of the results obtained so far, it appeared that, after the Fe^{2+} treatment, MnO NCs were either fully pristine (nonhollow) or completely hollow, that is, with no presence of intermediate structures in which the inner MnO core was partially etched or with reduced dimensions. This on-off feature of the hollowing process was observed not only by TEM, but also in the XRD analyses of the different MnO/SiO_2-xFe^{2+} samples: the crystal size of MnO domains, calculated via the Sherrer equation, was almost constant in the samples where MnO was present (i.e., from MnO/SiO_2-$5Fe^{2+}$ to MnO/SiO_2-$10Fe^{2+}$) (Table 1). These results suggest that, above the threshold for Fe incorporation inside the Mn_3O_4 shell (i.e., Fe ≥ 12 at. %), the Fe^{2+} cations triggered a sudden removal of the MnO core.

Such a hollowing process was also observed when exposing MnO NCs to other guest cations, such as Ce^{3+} and Fe^{3+}. Ce^{3+} can undergo a galvanic replacement with the Mn_3O_4 layer ($Mn(III) + Ce^{3+} \rightarrow Mn^{2+} + Ce(IV)$) forming CeO_2, due to the lower reduction potential of the Ce^{4+}/Ce^{3+} pair (i.e., 1.72 V) with respect to Mn_3O_4/Mn^{2+}. Indeed, after exposing MnO NCs to an excess of Ce^{3+} cation (4.5 times) dissolved in water, we observed the formation of hollow nanostructures containing both Ce and Mn species (sample named MnO/SiO_2-$450Ce^{3+}$, in Figure 4a and SI Figure S9). STEM-EDS analysis of the nonhollow NCs obtained after the Ce^{3+} treatment indicated that Ce was distributed mainly at the surface (SI Figure S9), indicating that also in this case the hollowing process started, possibly, with the galvanic replacement of Mn ions in the shell, and it proceeded with the removal of the MnO core.

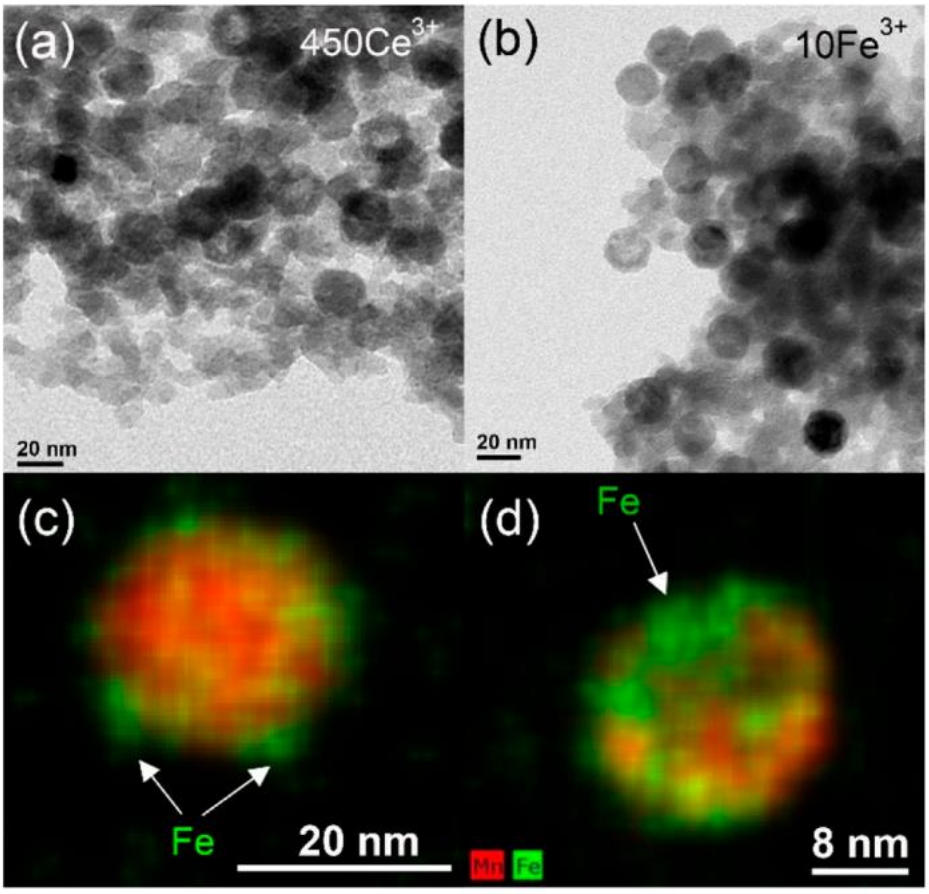

Figure 4. Bright field TEM images of MnO/SiO2 NCs treated with (a) excessive amount (4.5 times) of Ce3+ and (b) 10% of Fe3+ at room temperature. EDS-mapping of (c) a nonhollow NC and (d) a hollow NC, both belonging to the MnO/SiO2-10 Fe3+sample.

Working in a similar way, we exposed MnO NCs to Fe3+ cations, which cannot undergo galvanic replacement with Mn3O4 (the electrochemical potentials of these cations allow the galvanic replacement to occur only in the opposite direction, i.e., Mn(III) + Fe2+ → Mn2+ + Fe(III)). As Figure 4b reports, some of the MnO NCs were converted into hollow nanostructures containing both Fe and Mn elements. In this case, the Fe → Mn replacement is thought to occur via cation exchange of Mn3+ cations in the shell with Fe3+ in water.29 According to the general theory of cation exchange in NCs,29 the thermodynamic feasibility of a cation exchange process in water (or in polar solvents in general) can be predicted by comparing the solubility product constants (Ksp) of the starting and the product materials. In details, a material with a relatively high Ksp (more soluble) spontaneously transforms into another compound having a comparatively lower Ksp (less soluble) through cation exchange. Following this reasoning, the cation exchange reaction between

Mn3O4 and Fe3+ cations is thermodynamically favored since the solubility Ksp of the reaction product Fe3O4 (6.6 × 10-109) is much smaller than that of the starting Mn3O4 (7.1 × 10-55).30 Also in this case we did not observe the formation of heterostructures in which the core was partially etched, indicating that the hollowing process occurred in an on-off fashion.

It is worth noting that, even though the products obtained by employing either Fe2+, Ce3+, or Fe3+ are hollow nanostructures, the three experiments are characterized by different kinetics (i.e., the hollow structures are obtained by working with different host/guest cations ratios) and different structures. For instance, the cation exchange occurring with Fe3+ cations (i.e., in sample MnO/SiO2-10Fe3+) resulted in hollow structures in which the Fe and Mn cations were not homogeneously distributed (Figure 4c,d) compared to those produced via galvanic replacement (i.e., using Fe2+ cations). Also, different Fe/Mn cations ratios were required to convert all the NCs into hollow nanostructures: 30% in the case of Fe2+; 100% for Fe3+ (SI Figure S10). These results indicate that hollow structures can be synthesized by employing MnO NCs and following several different routes, each one delivering nanostructures with specific morphological and structural features. The choice of the guest cations plays a critical role: in a control experiment, we also tried using Co2+ which did not yield any obvious change in the morphology of MnO NCs (SI Figure S11).

We tried to understand the factors that drive the core removal process after the cation exchange/galvanic replacement occurring in the outer Mn3O4 layer. As revealed by the strain map in SI Figure S12, the strain built at the core-shell lattice interface increased with the increase of iron content in the shell. In detail, in the initial sample there was a lattice mismatch of 6.0% between the MnO core and the Mn3O4 shell. The increase in the Fe content from 4.0 at. % to 8.6 at. % resulted in a lattice mismatch between the Mn3-xFexO4 shell and the MnO core going from 8.8% to 10.9%. Moreover, according to the HRTEM analysis in SI Figure S13, when the content of iron reached 8.6%, both the core and shell lattices were already significantly distorted (i.e., rotated) to accommodate the mismatch, therefore creating many defects. This is indeed a common behavior found for core-shell particles to release the strain.31 We hypothesize that upon the incorporation of a certain amount of Fe cations, the lattice mismatch between the core and the shell increases, which in turn leads to the following: (i) the collapse of the MnO core; (ii) the formation of cracks and defects in the shell (SI Figure S13).

On the other hand, we exclude that the hollowing process is

due to a Kirkendall effect since that would lead to the formation of hollow structures whose wall thickness would be larger than the thickness of the starting Mn_3O_4 shell, which is not the case (the thickness of our nonhollow NCs was 3.9 ± 0.4 nm, while that of our hollow NCs was 3.7 ± 0.4 nm). In any case, a more in-depth research is required to fully understand this process.

The catalytic performance of the starting MnO and the Fe^{2+} treated samples were evaluated in the oxygen evolution reaction (OER) in 1 M KOH electrolyte. Three electrodes were prepared by depositing MnO NCs on a nickel foam (NF). Two of them were treated with Fe^{2+} aqueous solutions, similar to the case of MnO/SiO_2 discussed above. As a result, we obtained a total of three electrodes with varying concentrations of Fe^{2+} in the final product: MnO/NF, $Mn_{0.84}Fe_{2.16}O_4$/NF and $Mn_{0.36}Fe_{2.64}O_4$/NF (SI Figures S14-S16). The LSVs reported in Figure 5a show that the starting MnO/NF had an overpotential of 389 mV at 10 mA/cm^2, whereas the two Fe^{2+} exchanged samples, that is, $Mn_{0.84}Fe_{2.16}O_4$/NF and $Mn_{0.36}Fe_{2.64}O_4$/NF, exhibited overpotentials of 338 mV and 350 mV, respectively, at 10 mA/cm^2.

The Tafel slopes derived from the LSV curves markedly decreased from 95.2 mV/dec to 55.6 mV/dec and 43.3 mV/dec when the initial MnO/NF sample was converted to hollow NCs with compositions of $Mn_{0.84}Fe_{2.16}O_4$/NF and $Mn_{0.36}Fe_{2.64}O_4$/NF (Figure 5b), indicating that the Fe-doped hollow NCs had faster OER reaction kinetics than the nonhollow undoped one. It is also worth to note that the Tafel slope for $Mn_{0.36}Fe_{2.64}O_4$/NF is lower than most of the Mn_xO_y and Fe_xO_y based catalysts reported so far (a detailed comparison is reported in SI Figure S17).

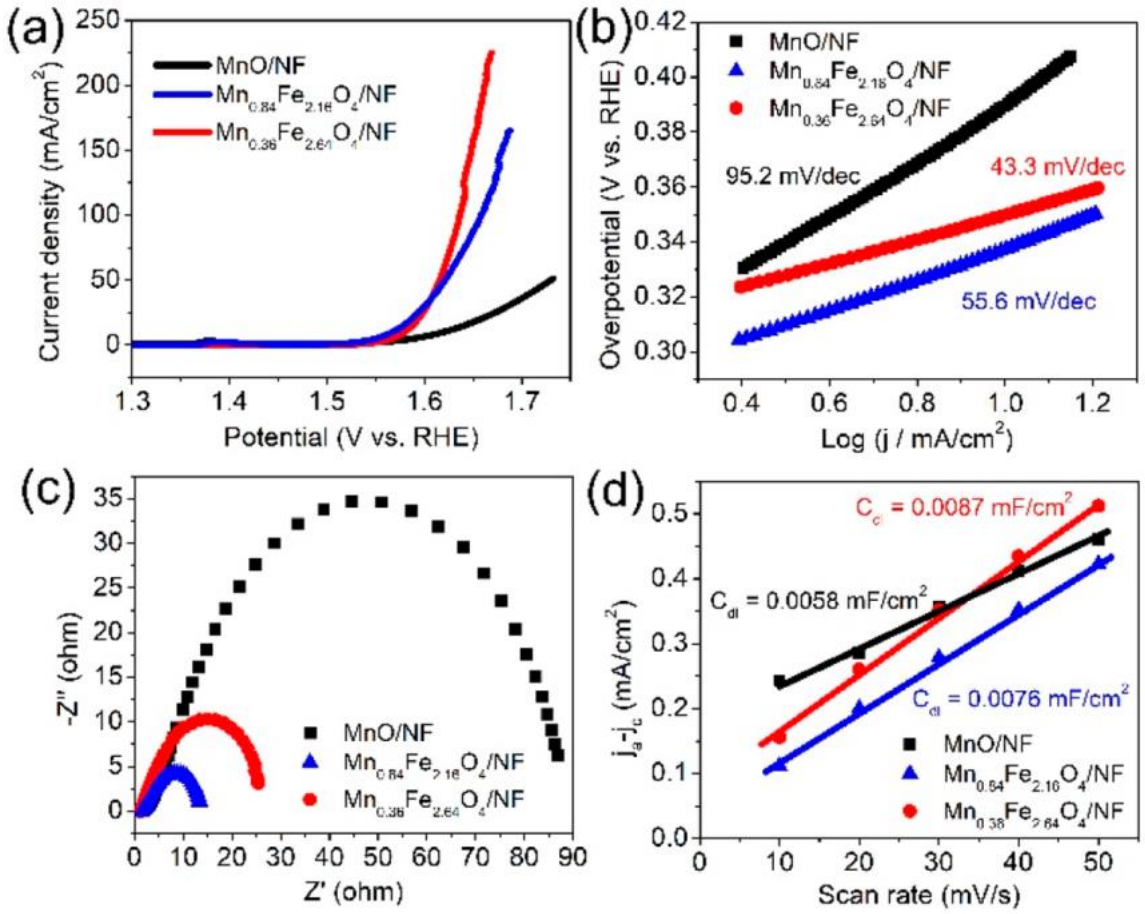

Figure 5. OER characterization results of the initial MnO/NF and two hollow samples after Fe2+ treatment, namely Mn0.36Fe2.64O4/NF and Mn0.84Fe2.16O4/NF: (a) LSVs and the corresponding (b) Tafel plots. (c) EIS Nyquist plots. (d) Calculation of double-layer capacitance (Cdl) based on the linear fitting of the capacitive currents of the catalysts vs the scan rates.

To understand the improvement induced by the Fe2+ treatment, we measured the conductivity and the electrochemical surface area (ECSA) of the three catalysts. The electrochemical impedance spectra (EIS) in Figure 5c showed a significant decline in the resistance after the Fe2+ treatment, which indicated a faster charge transfer. On the other hand, the ECSA obtained from electrochemical double layer capacitance (Cdl) in Figure 5d showed an increase from 0.0058 mF/cm2 to 0.0076 mF/cm2 (Mn0.84FeO4/NF) or to 0.0087 mF/cm2 (Mn0.36Fe2.64O4/NF), which was proposed to be highly related to the exposure of interior surface of NCs after the hollowing transformation.

■ CONCLUSION

In summary, we have developed a simple template-free method to prepare hollow Mn3-

xFexO4 NCs at room temperature. Upon exposure of preformed MnO NCs (deposited onto SiO2 and being characterized by a thin Mn3O4 shell) to an aqueous solution of Fe2+ cations, we observed a Fe2+ → Mn3+ galvanic replacement reaction initiated at the surface of the NCs. After a certain replacement threshold (12% of Fe in the shell region), we observed also the rapid removal of the MnO core which led to the formation of the final hollow nanostructures. Such Mn3-xFexO4 hollow NCs were tested in the electrocatalytic oxygen evolution reaction and demonstrated a significant improvement in activity with respect to starting MnO NCs, due to the rich electrochemical active surface sites and a fast charge transferability, caused by the Fe2+ triggered morphological and compositional changes. Our synthesis strategy can be potentially extended to other metal cations and exploited in various fields.

■ ASSOCIATED CONTENT

*sı Supporting Information

The Supporting Information is available free of charge at https://pubs.acs.org/doi/10.1021/acsanm.1c00819. TEM images, STEM-EDS images, SEM images, XRD patterns, TGA result, XPS analysis, and ICP results of various type of samples. Effect of reaction time. Size distributions of nonhollow and hollow NCs. Control experiment on fully oxidized Mn3O4/SiO2. Control experiment on ligand-free MnO/SiO2. Control experiment performed in an ethanol solution of Fe2+.

Experimental results using Ce3+, Fe3+ and Co2+ cations. Strain maps and HRTEM analysis of the defects in the shell. Acid etching experiment. Comparison of the OER overpotentials and Tafel slopes of our catalysts with the state-of-the-art catalysts in the literature (PDF).

■ AUTHOR INFORMATION

Corresponding Authors

Chunzheng Wu - College of Sciences, Zhejiang A&F University, Hangzhou, Zhejiang 311300, China; Department of Nanochemistry, Istituto Italiano di Tecnologia, 16163 Genova, Italy; orcid.org/0000-0001-9488-2224; Email: wucz@zafu.edu.cn

Zhiya Dang - School of Materials, Sun Yat-sen University, Guangzhou, Guangdong 510275, China; Department of Nanochemistry, Istituto Italiano di Tecnologia, 16163 Genova, Italy; Email: dangzhy3@mail.sysu.edu.cn

Luca De Trizio - Department of Nanochemistry, Istituto Italiano di Tecnologia, 16163 Genova, Italy; orcid.org/0000-0002-1514-6358; Email: luca.detrizio@iit.it

Authors
Lea Pasquale - Department of Nanochemistry, Istituto Italiano di Tecnologia, 16163 Genova, Italy
Mengjiao Wang - Materials Characterization Facility, Istituto
Italiano di Tecnologia, 16163 Genova, Italy
Massimo Colombo - Department of Nanochemistry, Istituto Italiano di Tecnologia, 16163 Genova, Italy; orcid.org/0000-0002-0817-0229
Liberato Manna - Department of Nanochemistry, Istituto Italiano di Tecnologia, 16163 Genova, Italy; orcid.org/0000-0003-4386-7985
Complete contact information is available at:
https://pubs.acs.org/10.1021/acsanm.1c00819
Notes
The authors declare no competing financial interest.
■ ACKNOWLEDGMENTS
We acknowledge the Starting Funding (2021FR027) from
Zhejiang A&F University and Starting Funding (76180-18841225) of “Hundred talents plan” from Sun Yat-sen University. We also acknowledge Dr. Rosaria Brescia from the
Electron Microscopy Facility of IIT for acquiring the STEMEDS mapping of Ce treated samples and Dr. Hongbo Yu from
Ningbo Institute of Materials Technology & Engineering
(CAS) for acquiring the SEM-EDS mapping of the three electrodes.
■ REFERENCES
(1) Prieto, G.; Tüysüz, H.; Duyckaerts, N.; Knossalla, J.; Wang, G.-H.; Schüth, F. Hollow Nano- and Microstructures as Catalysts. Chem. Rev. 2016, 116, 14056-14119.
(2) Wang, X.; Feng, J.; Bai, Y.; Zhang, Q.; Yin, Y. Synthesis,
Properties, and Applications of Hollow Micro-/Nanostructures.
Chem. Rev. 2016, 116, 10983-11060.
(3) Wu, C.; Dang, Z.; Prato, M.; Marras, S.; Cerea, A.; De Angelis, F.; Manna, L.; Colombo, M. Nanosized, Hollow, and Mn-Doped
CeO2/SiO2 Catalysts via Galvanic Replacement: Preparation,
Characterization, and Application as Highly Active Catalysts. ACS Applied Nano Materials 2018, 1, 1438-1443.
(4) Zhang, P.; Lu, X. F.; Luan, D.; Lou, X. W. Fabrication of
Heterostructured Fe2TiO5-TiO2 Nanocages with Enhanced Photoelectrochemical Performance for Solar Energy Conversion. Angew. Chem., Int. Ed. 2020, 59, 8128-8132.
(5) Wang, S.; Wang, Y.; Zang, S.-Q.; Lou, X. W. Hierarchical Hollow Heterostructures for Photocatalytic CO2 Reduction and Water Splitting. Small Methods 2020, 4, 1900586.
(6) Wan, X.-K.; Wu, H. B.; Guan, B. Y.; Luan, D.; Lou, X. W.
Confining Sub-Nanometer Pt Clusters in Hollow Mesoporous
Carbon Spheres for Boosting Hydrogen Evolution Activity. Adv.

Mater. 2020, 32, 1901349.
(7) Tang, Y.; Chen, S.; Mu, S.; Chen, T.; Qiao, Y.; Yu, S.; Gao, F. Synthesis of Capsule-like Porous Hollow Nanonickel Cobalt Sulfides
via Cation Exchange Based on the Kirkendall Effect for HighPerformance Supercapacitors. ACS Appl. Mater. Interfaces 2016, 8,
9721-9732.
(8) Zhang, J.; Li, Z.; Chen, Y.; Gao, S.; Lou, X. W. Nickel-Iron Layered Double Hydroxide Hollow Polyhedrons as a Superior Sulfur
Host for Lithium-Sulfur Batteries. Angew. Chem., Int. Ed. 2018, 57,
10944-10948.
(9) Fang, Y.; Yu, X.-Y.; Lou, X. W. Bullet-like Cu9S5 Hollow Particles
Coated with Nitrogen-Doped Carbon for Sodium-Ion Batteries.
Angew. Chem., Int. Ed. 2019, 58, 7744-7748.
(10) Lu, X. F.; Zhang, S. L.; Shangguan, E.; Zhang, P.; Gao, S.; Lou,
X. W. Nitrogen-Doped Cobalt Pyrite Yolk-Shell Hollow Spheres for
Long-Life Rechargeable Zn-Air Batteries. Advanced Science 2020, 7, 2001178.
(11) Shin, J.; Anisur, R. M.; Ko, M. K.; Im, G. H.; Lee, J. H.; Lee, I.
S. Hollow Manganese Oxide Nanoparticles as Multifunctional Agents
for Magnetic Resonance Imaging and Drug Delivery. Angew. Chem., Int. Ed. 2009, 48, 321-324.
(12) Xing, R.; Bhirde, A. A.; Wang, S.; Sun, X.; Liu, G.; Hou, Y.;
Chen, X. Hollow iron oxide nanoparticles as multidrug resistant drug
delivery and imaging vehicles. Nano Res. 2013, 6, 1-9.
(13) Varapragasam, S. J. P.; Balasanthiran, C.; Gurung, A.; Qiao, Q.;
Rioux, R. M.; Hoefelmeyer, J. D. Kirkendall Growth of Hollow
Mn
3O4 Nanoparticles upon Galvanic Reaction of MnO with Cu2+ and
Evaluation as Anode for Lithium-Ion Batteries. J. Phys. Chem. C 2017,
121, 11089-11099.
(14) Yang, R.; Fan, Y.; Ye, R.; Tang, Y.; Cao, X.; Yin, Z.; Zeng, Z.
MnO2-Based Materials for Environmental Applications. Adv. Mater.
2021, 33, 2004862.
(15) Ji, S.; Ma, Y.; Wang, H.; Key, J.; Brett, D. J. L.; Wang, R. Cagelike MnO2-Mn2O3 hollow spheres with high specific capacitance and
high rate capability as supercapacitor material. Electrochim. Acta 2016, 219, 540-546.
(16) Guo, X.; Li, J.; Jin, X.; Han, Y.; Lin, Y.; Lei, Z.; Wang, S.; Qin,
L.; Jiao, S.; Cao, R. A Hollow-Structured Manganese Oxide Cathode
for Stable Zn-MnO2 Batteries. Nanomaterials 2018, 8, 301.
(17) Ching, S.; Kriz, D. A.; Luthy, K. M.; Njagi, E. C.; Suib, S. L.
Self-assembly of manganese oxide nanoparticles and hollow spheres.
Catalytic activity in carbon monoxide oxidation. Chem. Commun.

2011, 47, 8286-8288.
(18) An, K.; Kwon, S. G.; Park, M.; Na, H. B.; Baik, S.-I.; Yu, J. H.; Kim, D.; Son, J. S.; Kim, Y. W.; Song, I. C.; Moon, W. K.; Park, H. M.; Hyeon, T. Synthesis of Uniform Hollow Oxide Nanoparticles through Nanoscale Acid Etching. Nano Lett. 2008, 8, 4252-4258.
(19) Oh, M. H.; Yu, T.; Yu, S.-H.; Lim, B.; Ko, K.-T.; Willinger, M.-G.; Seo, D.-H.; Kim, B. H.; Cho, M. G.; Park, J.-H.; Kang, K.; Sung, Y.-E.; Pinna, N.; Hyeon, T. Galvanic Replacement Reactions in Metal Oxide Nanocrystals. Science 2013, 340, 964-968.
(20) Wu, C.; Brescia, R.; Prato, M.; Marras, S.; Manna, L.; Colombo, M. Tuning the CO oxidation catalytic activity of supported metalmetal oxide heterostructures by an aqueous phase post-treatment process. J. Mater. Chem. A 2016, 4, 18075-18083.
(21) López-Ortega, A.; Roca, A. G.; Torruella, P.; Petrecca, M.; Estradé, S.; Peiró, F.; Puntes, V.; Nogués, J. Galvanic Replacement onto Complex Metal-Oxide Nanoparticles: Impact of Water or Other Oxidizers in the Formation of either Fully Dense Onion-like or Multicomponent Hollow MnOx/FeOx Structures. Chem. Mater. 2016, 28, 8025-8031.
(22) Yin, Y.; Rioux, R. M.; Erdonmez, C. K.; Hughes, S.; Somorjai, G. A.; Alivisatos, A. P. Formation of Hollow Nanocrystals Through the Nanoscale Kirkendall Effect. Science 2004, 304, 711-714.
(23) Tian, L.; Yang, X.; Lu, P.; Williams, I. D.; Wang, C.; Ou, S.; Liang, C.; Wu, M. Hollow Single-Crystal Spinel Nanocubes: The Case of Zinc Cobalt Oxide Grown by a Unique Kirkendall Effect. Inorg. Chem. 2008, 47, 5522-5524.